

Origin of Performance Enhancement in TiO₂-Carbon Nanotube Composite Perovskite Solar Cells

*Thomas J. Macdonald**, Munkhbayar Batmunkh, Chieh-Ting Lin, Jinhyun Kim, Daniel D. Tune, Filip Ambroz, Xiaoe Li, Shengda Xu, Christian Sol, Ioannis Papakonstantinou, Martyn A. McLachlan, Ivan P. Parkin, Joseph G. Shapter, James R. Durrant

Dr. T.J. Macdonald, F. Ambroz, Prof. I.P. Parkin
Department of Chemistry, University College London, 20 Gordon St, London, WC1H 0AJ,
United Kingdom
E-mail: tom.macdonald@ucl.ac.uk

Dr. M. Batmunkh, Prof. J.G. Shapter
Australian Institute for Bioengineering and Nanotechnology, The University of Queensland,
St Lucia, Queensland, 4072, Australia

C-T. Lin, S. Xu, Dr. M.A. McLachlan
Department of Materials and Centre for Plastic Electronics, Imperial College London,
Imperial College Road, London, SW7 2AZ, United Kingdom

C-T. Lin, J. Kim, Dr. X. Li, Prof. J.R. Durrant
Department of Chemistry and Centre for Plastic Electronics, Imperial College London,
Imperial College Road, London, SW7 2AZ, United Kingdom

Dr. D.D. Tune
Institute of Nanotechnology, Karlsruhe Institute of Technology, 76021 Karlsruhe, Germany

C. Sol, Prof. I. Papakonstantinou
Department of Electronic and Electrical Engineering, University College London, Torrington
Place, London, WC1E 7JE, United Kingdom

Prof. J.R. Durrant
SPECIFIC IKC College of Engineering, Swansea University, Swansea, SA2 7AX, United
Kingdom

Keywords: carbon nanotubes, perovskite solar cells, device performance, titanium dioxide,
cnts

Carbon nanotubes have been shown to be beneficial additives to perovskite solar cells, and the inclusion of such nanomaterials will continue to play a crucial role in the push towards developing efficient and stable device architectures. Herein, titanium dioxide/carbon nanotube composite perovskite solar cells are fabricated, and device performance parameters are correlated with spectroscopic signatures of the materials to understand the origin of performance enhancement. By probing the charge carrier dynamics with photoluminescence and femtosecond transient absorption spectroscopy, the results indicate that charge transfer was not improved by the presence of the carbon nanotubes. Instead, carbon nanotubes are shown to passivate the electronic defect states within the titanium dioxide, which can lead to stronger radiative recombination in the titanium dioxide/carbon nanotube films. The defect passivation allows the perovskite solar cells made using an optimized titanium dioxide/carbon nanotube composite to achieve a peak power conversion efficiency of 20.4% (19% stabilized), which is one of the highest values reported for perovskite solar cells not incorporating a mixed cation light absorbing layer. The results discuss new fundamental understandings for the role of carbon nanomaterials in perovskite solar cells and present a significant step forward in advancing the field of high-performance photovoltaics.

1. Introduction

Carbon nanotubes (CNTs) are a class of 1D nanomaterials consisting of very high aspect ratio cylinders of sp^2 hybridized carbon and possess a unique suite of exceptional physical properties making them ideally suited to a wide range of applications throughout materials science and optoelectronics. In many ways this materials class bridges the divide between the solid-state world of bulk crystalline semiconductors on the one hand, and the newer field of organic electronics on the other, whilst exhibiting desirable characteristics and solving fundamental limitations of both. In regards to electronics, the outstanding properties of charge carriers in single-walled carbon nanotubes (SWCNTs) spurred early explorations of CNT field-effect

transistors (FETs)^[1] and nanotube-nanotube linear^[2] and crossed junctions,^[3] whilst more recent work has demonstrated CNT-FETs with switching speeds that are now comparable to, or even exceeding, those of conventional Si CMOS.^[4] In terms of optoelectronics, light emission from CNTs has been coupled into photonic waveguides providing essential elements of future quantum information processing platforms,^[1] and diazonium chemistry can now be used to engineer single point defects in CNT sidewalls to provide very high quality single photon sources.^[2] Aside from their attractive optoelectronic characteristics, a further advantage of CNTs is their extreme chemical, mechanical and thermal stability,^[5–8] especially when compared to their small molecule and polymer organic cousins. This stability enables them to be used for greatly extended periods of time and is particularly advantageous in regard to their application in photovoltaics.

Since their discovery, CNTs have been incorporated into many photovoltaic architectures, and in a variety of roles within them. For example, as early as 1999, an organic polymer device made with multiwalled carbon nanotubes (MWCNTs) as the hole collecting electrode was found to demonstrate nearly twice the quantum efficiency of standard indium tin oxide devices.^[9] The improvement was attributed to better energy transfer onto the nanotubes, as well as a larger interfacial area. Later, SWCNTs were incorporated into the titanium dioxide (TiO₂) electron-transport layer (ETL) of dye-sensitized solar cells (DSSCs), resulting in an enhancement in the photocurrent which was attributed to an improvement in electrical conductivity, light scattering, and the concentration of free conduction band electrons.^[10] This was followed by work incorporating SWCNTs into the counter electrodes of DSSCs,^[11] as transparent electrodes in flexible polymer solar cells^[12] and in nanotube/silicon heterojunction solar cells,^[13] as well as primary absorbers of light in donor-accepter complex with fullerenes.^[14,15] Whether they are used as simple electrodes, as electron or hole transporting

layers, or as absorbers, the literature demonstrates great potential for the use of CNTs as beneficial additives in solar devices.^[16–18]

To add to this broad family of photovoltaics, recent advancements in perovskite solar cells (PSCs) have also shown distinct performance enhancements from CNTs.^[19–25] Emerging PSCs distinguish themselves as excellent candidates for third generation photovoltaics due to their efficient light absorption, tunable band gaps, and low material cost.^[26] A majority of studies on CNTs in PSCs exploit their use in the hole transport material (HTM) or as a counter electrode due to the inherent *p*-type character of air-exposed SWCNTs. Previous work by Habisreutinger et al. has shown that SWCNTs can also be used as *p*-type dopants in Spiro-MeTAD to replace the common dopants 4-tert-Butylpyridine (tBP) and the hydroscopic Bis(trifluoromethane)sulfonimide lithium salt (LiTFSI).^[19] Furthermore, the combination of two separate 1-D materials, such as nanofibers and nanotubes, has also been shown to improve performance.^[27,28] CNTs can also be used in the ETL and despite this being somewhat counterintuitive when considering only the slightly *p*-type character of the CNTs, this nevertheless results in clear improvements in overall device performance.^[21,28,29] Previous reports have suggested that the CNTs could improve electron mobility and directionality,^[27,31] however further research is required to fully understand the mechanism of this system. While clear evidence of improved charge transfer has been shown at the interface between pure SWCNT contacts and a methylammonium lead iodide (MAPbI₃) absorber layer,^[32] an understanding of the performance enhancement achieved when these two materials are combined as a composite material in PSCs is still lacking.

Therefore, in the present study, we fabricated PSCs with CNTs in the ETL as illustrated in Scheme 1. The conventional architecture was chosen since the most efficient PSCs are still fabricated using TiO₂ as the ETL.^[33] We use MAPbI₃ as our test system since, while significant

advances in stability have been made with mixed cation perovskites,^[34] there have also been recent reports of impressive MAPbI₃ stability,^[35] and MAPbI₃ is still the most widely studied perovskite material with the most thoroughly investigated fundamental properties. We consider the effects of photoinduced charge transfer across the TiO₂-CNT and MAPbI₃ interface by steady-state photoluminescence, time correlated single photon counting (TCSPC) and femtosecond transient absorption spectroscopy (fs-TAS), utilizing spectroscopic signatures for TiO₂-CNTs and MAPbI₃. Interestingly, we show that adding CNTs to metal oxide photoelectrodes does not necessarily result in an improved electron transfer between MAPbI₃ and TiO₂, as we suggested in our preliminary work.^[21] We instead present evidence that CNTs are able to passivate the electronic defect states in the TiO₂, which leads to stronger radiative recombination in the TiO₂-CNT photoelectrodes, and thus the improvement in device performance.

2. Results and Discussion

Our conventional PSC device architecture can be seen in scheme 1. Devices with and without CNTs in the ETL were fabricated, and their photovoltaic parameters were measured under AM1.5G illumination. The CNT loading in the ETL was 0.1 wt% as per the concentration optimizations from our previous report and the presence of CNTs was confirmed by Raman Spectroscopy as shown by the characteristic D and G-bands in Figure S1 in the supplementary information.^[21] The current density voltage (*J-V*) characteristics of the highest performing TiO₂-CNT and TiO₂ based photoelectrodes are displayed in Figure 1 (a) and their corresponding *J-V* parameters are shown in Table 1, along with the average values from 76 devices (38 of each type). As per our previous reports, the photoelectrodes made from the TiO₂-CNT composite all showed improved performance compared to the TiO₂ controls.^[20,21] The highest PCE measured was 20.4 % (19 % stabilized) and 18.4 % (17 % stabilized) for the TiO₂-CNT and TiO₂ PSCs respectively. Figure 1 (b) shows the steady-state PCE, where the devices were held near their

maximum power point (MPP) for 200 s. Our previous work has shown a significant reduction in hysteresis for photoelectrodes containing CNTs^[21] and this supports our results observed from the steady-state efficiency measurements (Figure 1 (b)). Measurement of the steady-state efficiency of PSCs is essential to accurately quantify performance since, as argued in a recent report by Habisreutinger et al., the widely used hysteresis index only represents a transient state in a PSC. However, since hysteresis is still a frequently discussed topic in PSCs, a forward-reverse scan for the TiO₂-CNT device has been provided in Figure S2 (b) showing minor hysteresis, as expected for the combination of TiO₂ and MAPbI₃.^[37]

The performance enhancement was first evaluated by analysing the improved photovoltaic parameters (J_{SC} , V_{OC} , and FF). To confirm the J_{SC} enhancement, Figure 1 (c) shows the incident-photon-to-current-efficiency (IPCE) measurements with and without CNTs. The integrated J_{SC} was 21.6 mA cm⁻² and 20.4 mA cm⁻² for the TiO₂-CNT and TiO₂ PSCs, which is in close agreement with the average values in Table 1. The small discrepancy (~6 %) between the J_{SC} and the integrated current calculated from the IPCE measurements was partly attributed to the mesoporous layer contributing to a photocurrent barrier which is typically larger at low light intensities, along with a contribution from the capacitive current present in linear sweep J - V curves.^[38,39] Other factors influencing the small discrepancy can be related to optical losses from reflection and/or slow photocurrent responses.^[38] We note that our TiO₂-CNT and TiO₂ layers were both doped with LiTFSI, since Li-doped TiO₂ photoelectrodes have been shown to exhibit superior electronic properties due to passivation of electron defect states enabling faster electron transport.^[40] To determine whether or not the trend in performance enhancement was still observed without Li-doping, PSCs were made using TiO₂-CNT and TiO₂ photoelectrodes without LiTFSI treatment. The J - V curves and photovoltaic parameters are shown in Figure S2 (a) and Table S1 of the Supporting Information (SI) and confirm the same trend as for the Li-doped devices. While the average J - V parameters were consistently higher for the PSCs made

with CNTs, the overall difference in performance without LiTFSI treatment can be seen in the lower V_{oc} , consistent with previous reports.^[40]

Electrochemical impedance spectroscopy (EIS) was carried out to evaluate the charge recombination dynamics. Figure 1 (d) shows the Nyquist plots obtained from TiO₂-CNT and TiO₂ PSCs measured under illumination ranging from 1 Hz to 100 kHz at open-circuit conditions. Figure 1 (d) represents the equivalent circuit which was adopted from literature to fit the Nyquist spectra and Figure S2 (c) shows a more resolved representation of the experimental fits for the main arch of the spectra.^[41] Previous reports have ascribed the first semicircle in the mid frequency region to the impedance arising from electron transport where a smaller circle indicates a lower charge transfer resistance at the perovskite interfaces.^[41] The first semicircle closest to the origin can be ascribed to impedance arising from electronic transport.^[41,42] On the other hand, double layer capacitance^[43] or charge accumulation^[44] mechanisms have been proposed for the formation of the semicircle in the low frequency region. Bag et al. later proposed that a linear region (between the two semicircles) can be ascribed to charge accumulation from ionic diffusion (Warburg diffusion) as well as ion migration.^[45] The linear slopes on the incomplete semicircles in the low frequency region is strong evidence that the impedance in these devices arises due to Warburg ion diffusion i.e. the migration of alkylammonium ions, with Warburg impedances of 0.24 Ω and 0.37 Ω calculated from slopes of TiO₂-CNTs and TiO₂ PSCs, respectively.^[41,45] The corresponding series resistance (R_s), recombination resistance (R_{rec}), chemical capacitance ($C_{\mu, mf}$), and lifetimes (τ) of the PSCs extracted by modelling the EIS data according to the equivalent circuit shown in Figure 1 (d) are shown in Table S2 of the SI and demonstrate significantly improved electrochemical performance of the PSCs containing the CNTs. First, a 10 % reduction in R_s indicates easier electron transport through the TiO₂-CNT PSCs. Second, the main arc in the mid frequency region of the EIS is indicative of R_{rec} , which is inversely proportional to the recombination rate

within the device.^[46] The R_{rec} of TiO₂-CNT and TiO₂ PSCs was 1.60 k Ω and 1.39 k Ω , respectively, which suggests that the PSCs with the CNTs have an increased steady state electron density, which in turn supports a higher V_{oc} .^[47] We also calculate a 9 % lower $C_{\mu,\text{mf}}$ in the devices with the CNTs, indicating that the CNTs act to reduce charge storage in sub-bandgap states within the TiO₂, and could also contribute to the improved V_{oc} .^[48] Previous reports on mesoporous PSCs have linked the rate of recombination events to the thickness of the mesoporous layer, which results in a decrease in electron diffusion length.^[49] Since the thicknesses of our mesoporous layer for the TiO₂ and TiO₂-CNT photoelectrodes were the same, we attribute the increase in recombination resistance to the presence of the CNTs. In one possible model, the presence of the CNTs reduces the trap defect density in the TiO₂, which subsequently reduces the quenching of carriers photogenerated in the MAPbI₃. Similar trends have been reported whereby reducing such defects in the TiO₂ has been found to reduce the series resistance and increase the FF of PSCs, which is consistent with our results from the J - V curves.^[50–52]

The main contributor to the increase in efficiency was the improvement in average J_{sc} (~ 6 %) across all PSCs containing the CNTs. Histograms showing the J_{sc} and PCE of a total of 76 individual PSCs are shown in Figure 2 (a, d). The histograms show a clear trend of improved parameters amongst all devices containing CNTs, illustrating good reproducible performance enhancement. An independent samples t-test revealed the improved photovoltaic parameters were statistically significant ($P < 0.001$). Histograms showing the V_{oc} and FF values across 76 PSCs are shown in Figure 2 (b, c), again illustrating considerable improvements with PSCs containing CNTs. The combination of improved parameters resulted in consistently higher PCE for all devices containing the CNTs as shown in Figure 2 (d). The average values for all devices shown in the histograms is displayed in Table 1. The stability of the PSCs was also investigated by leaving the devices under constant 1 sun illumination for ~16 h and periodically running J -

V curves to monitor the performance. The degradation of device performance was reduced by the addition of CNTs, as shown in Figure S3 of the SI, consistent with previous reports.^[21] Previous simulation studies show that MAPbI₃ undergoes a rapid solvation process in a liquid water environment,^[53] which suggests it would be useful to provide a barrier layer assisting in preventing or slowing down the degradation of the perovskite. In our work, we attribute the enhanced stability to the addition of CNTs resulting in an increase in hydrophobicity on the TiO₂ ETL as shown from the contact angle measurements in Figure S2 (d). Increasing the hydrophobicity of the ETL will result in lower amounts of moisture in the electrode and hence less degradation of the MAPbI₃. Similar phenomena in increased stability from carbonaceous nanomaterials have been reported before whereby their presence has been thought to create a barrier layer, which assists in blocking the contact between water and MAPbI₃.^[54] Additionally, it is well known the CNTs are able to soak radical oxygen,^[55] which means any molecular oxygen adsorbed on the TiO₂ could be adsorbed by the CNTs, further improving the stability.^[21,56] The average shunt (R_{sh}) and series (R_s) resistance were also extracted from the *J-V* curves of all 76 PSCs (Table S3, SI). While there was only a slight improvement, the trends in the average R_s with our photovoltaic parameters are all consistent with the enhanced performance for the CNT containing PSCs. The decreased average R_s was also consistent with the results from the EIS (Table S2). The average R_{SH} values were 9.9×10^3 and $3.0 \times 10^3 \Omega \text{ cm}^2$ for the and TiO₂-CNT and TiO₂ PSCs respectively. The average R_{SH} were more than three times lower for the control devices, which is consistent with the lower average *FF* measured in the devices without CNTs. Dark *J-V* measurements were performed to better understand the diode behaviour. The saturation-current (J_{sat}) and ideality factor were extracted from the semi-log plots of the dark *J-V* data shown in Figure 3 (a, b). The average J_{sat} for the CNT containing PSCs was on the order of $10^{-10} \text{ mA cm}^{-2}$, which was 3 orders of magnitude lower than the control devices, allowing for a higher V_{oc} under illumination. The average ideality factor was calculated to be 1.55 and 1.91 for the TiO₂-CNT and TiO₂ PSCs, respectively. The substantially

lower J_{sat} and ideality factor obtained for the TiO₂-CNT PSCs is indicative of better diode performance, and correlates well with the higher R_{rec} and lower $C_{\mu,\text{mf}}$ measured in EIS. The absence of a minimum current density at 0 V may be attributed to two reasons. Firstly, a small imperfection in the dark enclosure which could allow the equivalent of 0.1-0.2 % of the AM1.5G intensity into the enclosure. Secondly, the accumulation of charges due to the mobile ions at the perovskite interface can lead to a displacement current which can be attributed to J - V hysteresis.^[57,58] Despite this, we do not believe that this qualitatively changes the results of our comparisons between the TiO₂ and TiO₂-CNT devices, in particular, the three orders of magnitude decrease in saturation current density upon inclusion of the CNTs. In addition, the scan rates for the PSCs were kept constant meaning that any effect on ion movement influenced by the scan rate would be relative between all both TiO₂ and TiO₂-CNT PSCs.

To obtain more information about the origin of the enhanced device performance, TiO₂ and TiO₂-CNT sol-gel solutions were spin coated onto 15 Ω fluorine doped tin oxide (FTO) glass substrates for optical characterisation. FTO and cp-TiO₂ was included in the preparation of the photoelectrodes to best emulate the PSCs. The TiO₂-CNT composite material contained 0.1 wt% SWCNT which yielded a grey sol-gel, the exact experimental procedure can be found in the experimental section. Figure 4 (a) shows the specular reflectance spectra of TiO₂-CNT and TiO₂ substrates where a broad reduction in reflectance is observed for wavelengths longer than approximately 350 nm for the sample containing the CNTs, possibly indicating a contribution from absorption scattering by the CNTs. This can also be observed as a visible darkening of the sol-gel color when compared to the control TiO₂ sol-gel solution as shown in Figure S4. The inset in Figure 4 (a) show Tauc plots of the absorption spectra (shown in full Figure S5 (a) of the SI) of TiO₂ and TiO₂-CNT photoelectrodes, showing no significant shift in bandgap, although previous work has shown a significant red shift in absorption edge for TiO₂-CNT (1.0 wt% CNT) composite materials.^[59] We attributed the lack of a shift in our devices to the fact

that the amount of CNTs (0.1 wt%) was too small to have a noticeable effect. The results indicate that the bandgap of the TiO₂ and TiO₂-CNT photoelectrodes was 3.35 eV, which is in good agreement with reported values for TiO₂.^[60] The lack of a shift in the conduction band of the TiO₂-CNT precludes this is a contributor to the slight increase in V_{oc} . More specifically, this suggests that any improvement in V_{oc} is likely coming from surface effects of the TiO₂-CNT or contact between the TiO₂-CNT and MAPbI₃ layer. Previous work shows that ETL layers made from crosslinked fullerenes have the potential to improve both V_{oc} and FF in PSCs.^[61] This further supports the likelihood that the effects we observe are not correlated to any shift in conduction band of the TiO₂. The diffuse reflectance spectra also showed a similar trend in a decrease in reflectance at 365 nm for the CNT sample, albeit with the expected reduction in overall intensity, and is shown in Figure S5 (b) in the SI.

The complex refractive index of the TiO₂ and TiO₂-CNT photoelectrodes were then measured by ellipsometry. The variation of the real and imaginary parts with wavelength are shown in Figure 4 (b) where the samples containing the CNTs have a larger refractive index and extinction coefficient across the visible region. A distinct increase can be seen from 350 – 800 nm in the extinction coefficient of TiO₂-CNT photoelectrodes, which explains the reduced reflectance measured observed in this range. The thickness of the TiO₂ layers in this work was matched with that typically used in a PSC (150 nm). Since the complex refractive index of TiO₂ is thickness dependent,^[62] ellipsometry of a significantly thinner layer (~ 15-20 nm) was also performed. Figure S5 (c) in the SI again shows a change in the complex refractive index with the inclusion of CNTs and confirms that even with varying thickness, the extinction coefficient was increased across the visible region.

After deposition of MAPbI₃ onto TiO₂ and TiO₂-CNT photoelectrodes *via* the adduct approach,^[63] the absorbance of MAPbI₃, TiO₂/MAPbI₃, and TiO₂-CNT/MAPbI₃ on FTO was

measured and is plotted in Figure 4 (c). The results show that while the absorptance was similar, the composite photoelectrode containing the CNTs shows the highest total absorptance, where integrating under the curves showed an average of 2 % improvement in total absorptance which can be linked with the higher J_{sc} observed in the PSCs. However, it cannot explain the 6 % improvement in J_{sc} , meaning that there must be other factors contributing to the improvement. In order to investigate whether the CNTs had any influence on the topography of the TiO₂ and MAPbI₃ crystallization, scanning electron microscopy (SEM) was performed. SEM images of TiO₂, TiO₂-CNT, TiO₂/MAPbI₃, and TiO₂-CNT/MAPbI₃ are shown in Figure S6 (a-d) in the SI, confirming that the CNTs had no noticeable influence on the topography of either TiO₂ or MAPbI₃. To determine whether or not the CNTs had any influence on the crystallization of MAPbI₃, X-ray diffraction (XRD) was performed on MAPbI₃, TiO₂/MAPbI₃, and TiO₂-CNT/MAPbI₃ photoelectrodes and shows no shift or broadening of any of the associated XRD signatures for MAPbI₃ (Figure S7).^[64]

In order to investigate the charge carrier dynamics at the interface between TiO₂-CNT and MAPbI₃, photoluminescence (PL) spectroscopy was used to probe the photoexcited states in the TiO₂-CNT/MAPbI₃ photoelectrodes. Steady state PL measured using a filtered white light emitting diode (LED) excitation source with 1 sun equivalent fluorescence^[65] is shown in Figure 4 (d). The relative rates of charge transfer from the MAPbI₃ to the active TiO₂ and TiO₂-CNT layers can be assessed by calculating the PL quenching efficiency (PLQE) as represented in equation 1, where I_0 is the peak intensity of PL emission of MAPbI₃, and I is the peak intensity of PL emission of the perovskite with transport layers (TiO₂ /MAPbI₃ and TiO₂-CNT/MAPbI₃).

$$PLQE(\%) = \frac{I_0 - I}{I_0} * 100 \% \quad \text{Equation 1}$$

Interestingly the PLQE of TiO₂/MAPbI₃ is 77 % compared to 66 % for the TiO₂-CNT/MAPbI₃, where the higher quenching efficiency entails a more efficient charge transfer from MAPbI₃ to TiO₂ (compared to TiO₂-CNT) due to efficient non-radiative processes. We note that our previous report showed more effective PL quenching from TiO₂-CNT/MAPbI₃ photoelectrodes.^[21] We attribute this to the fact that our previous study employed a different MAPbI₃ deposition technique with little control over crystallization kinetics, resulting in less-uniform MAPbI₃ films with smaller grain sizes. The grain boundaries formed around the smaller MAPbI₃ crystals were therefore in close proximity to the ETL and the CNTs within it, facilitating the PL quenching. However, this work used the adduct approach to produce highly uniform and crystalline MAPbI₃ films with large grains as shown in Figure S6 (c and d). This means that the grain boundaries are on average, further from the CNTs and are thus playing less of a role in the PL quenching due to the high uniformity and large crystal size of the MAPbI₃ films.^[66]

To better understand the PL decay kinetics of the TiO₂-CNT/MAPbI₃ photoelectrodes, time correlated single photon counting (TCSPC) with an excitation of 635 nm and probe of 770 nm was performed. Figure 4 (e) shows the TCSPC spectra, which were fitted with a biexponential (Equation 2) where the fast decay phase (monomolecular) can be linked with trap-assisted processes (τ_1 , surface component), and the slow decay phase (bimolecular) represents recombination of the free charge carriers (τ_2 , bulk component).^[67,68] In addition, the relative contributions of both the surface and bulk components were quantified by integrating the respective exponential traces.^[67] The amplitude (real time), PL decay kinetics and their relative contributions for MAPI, TiO₂/MAPbI₃, and TiO₂-CNT/MAPbI₃ are shown in Table 2.

$$y = y_0 + A_1 e^{-\frac{x}{\tau_1}} + A_2 e^{-\frac{x}{\tau_2}} \quad \text{Equation 2}$$

For the surface component (τ_1), the MAPbI₃ film shows a decay time of 0.85 ns, which was decreased to 0.58 ns and 0.73 ns for the TiO₂/MAPbI₃ and TiO₂-CNT/MAPbI₃ photoelectrodes, respectively. The decrease in decay time for the photoelectrodes containing the ETL can be attributed to electron transfer from the MAPbI₃ onto the TiO₂ or TiO₂-CNT. In comparison to TiO₂/MAPbI₃ photoelectrode, the 25 % increase in decay time for the surface component (τ_1) of the TiO₂-CNT/ MAPbI₃ photoelectrode suggests that charge transfer is not enhanced by the CNTs, also consistent with the steady-state PL spectra. We then consider the bulk component (τ_2) to assess the recombination of the free charge carriers. The bulk decay component was measured to be 380 ns for MAPbI₃ and was decreased to 60 ns and 97 ns for the TiO₂/MAPbI₃ and TiO₂-CNT/MAPbI₃ photoelectrodes, respectively, as expected due to the smaller grain size in the mesoscopic system resulting in efficient charge extraction.^[69] The longer lifetime (τ_2) for TiO₂-CNT/MAPbI₃ photoelectrode compared to TiO₂/MAPbI₃ photoelectrode suggests a slower rate of bimolecular recombination, which is consistent with the observations in our PL studies. Since the surface component (τ_1) amounts to 17.6 % of the total fit for the TiO₂-CNT/MAPbI₃ films and 15.4 % for the TiO₂/MAPbI₃ films, this also suggests that the CNTs are playing a larger role in passivating trap states in the photoelectrodes. Together with the increased lifetime, the results suggest that CNTs are able to passivate electronic defect states acting as nonradiative recombination centres in the TiO₂, and we propose that this leads to stronger radiative recombination in the TiO₂-CNT/MAPbI₃ photoelectrodes.^[61]

In an attempt to try and locate any elemental signs of defect passivation of the TiO₂, x-ray photoelectron spectroscopy (XPS) was performed on TiO₂ and TiO₂-CNT photoelectrodes. Figure S8 (a,b) shows the unchanged Ti2p spectra for both TiO₂ and TiO₂-CNT photoelectrodes respectively. Although no changes are observed, this is more than likely due to the small loading of CNTs (0.1 wt %) or the high temperature treatment of the photoelectrodes masking any

effects of functionality. Although changes in defect states in the TiO₂ were not detectable by XPS, we expect that any electronic changes induced by the CNTs were so small that it is beyond the detection limit of the XPS. Future work will incorporate hard XPS to reveal more information from the deep core of the photoelectrodes. In support of these future studies, previous work revealing electronic and atomic structure of modified TiO₂ has been best achieved using a combination of hard XPS and first-principles density functional theory calculations.^[70]

In order to further elucidate the passivation effects of the CNTs, we would like to highlight that the P3 CNTs from Carbon Solutions are functionalised with carboxylate groups (carboxylate-CNTs) which is experimentally known to occur at the sidewalls and ends of the CNTs.^[71] Previous theoretical simulations have investigated the potential physical and chemical adsorption sites for anatase TiO₂ and carboxylate-CNTs. They report that while adsorption sites depend on the geometry of the adsorbate and direction of orientation, for anatase TiO₂, preferential chemisorption occurs at the edges of the carboxylate site.^[72] Although our CNT loading was low (0.1 wt %) and the carboxylate groups will more than likely be removed upon heat treatment, this has still clearly resulted in an interaction (initially) between the CNTs and the TiO₂. On the basis of previous experimental and theoretical studies, we postulate that passivation occurs by interactions between the CNTs and the TiO₂ nanoparticles. However, further studies regarding the underlying mechanism of this interaction (whether that be by charge transfer or chemical bond) remains ongoing.

To further verify the observations from the PL decay kinetics, we now turn our attention to femtosecond transient absorption spectroscopy (fs-TAS), which is an optical technique used to determine the charge transfer properties in perovskite devices. Here, fs-TAS was used to confirm the higher rate of charge transfer observed in the PL and PL decay kinetics of the

TiO₂/MAPbI₃ films. Figure 4 (f) shows the dynamics of the decay kinetics for MAPbI₃, TiO₂-MAPbI₃, and TiO₂-CNT/MAPbI₃ films probed at 755 nm. The optical density change (ΔOD) at 755 nm can be attributed to the low energy photo bleaching, which is assigned to the band edge transition of MAPbI₃.^[73] The decay for TiO₂-MAPbI₃ (5.7 ns) was clearly faster than the decay for TiO₂-CNT/MAPbI₃ (8.6 ns), further supporting the faster electron transfer for the TiO₂/MAPbI₃ films in contrast to the TiO₂-CNT/MAPbI₃ films. Taken together, the results from the PL, TCSPC, and fs-TAS show that electron transfer is not necessarily improved by the presence of CNTs. Rather, the results combine to show that non-radiative decay *via* trap states at the interface is suppressed in the presence of the CNTs. Thus, we postulate that the CNTs act to passivate those trap states, reducing the overall level of recombination in the devices and providing a physical basis for the observed increase in **FF** and reduction of saturation current/increase in V_{oc} . Since the average J_{sc} was improved by ~ 6 % but the total absorptance was improved by only 2 %, we conclude that this reduced recombination contributed to a 4 % improvement in J_{sc} .

3. Conclusion

In this work, we fabricated conventional PSCs on a mesoporous TiO₂-CNT composite, achieving a maximum conversion efficiency of 20.4% compared to 18.4% for control devices made without CNTs. The devices showed an improvement in J_{sc} which can be attributed to an increase in absorptance. Through modelling of the impedance spectra, we showed that the presence of CNTs improves the recombination resistance, suggesting an increase in steady state electron density, and simultaneously reduces the chemical capacitance. Interestingly, by probing the transient behaviour of charge carriers with PL, TCSPC, and fs-TAS, our results suggest that the charge transfer between MAPbI₃ and TiO₂-CNT was not improved compared to TiO₂, but rather that the CNTs are able to passivate electronic defect states in the TiO₂. The

passivation of interface recombination in the photoelectrodes causes the increase in recombination resistance and 3 orders of magnitude decrease in saturation current, which in turn provide an increase in FF and V_{oc} as seen in the $J-V$ data. The results suggest that the origin of performance enhancement for TiO_2 -CNT PSCs can be predominantly linked with increased light absorption and reduced recombination. We highlight that the CNTs are clearly beneficial additives to the mesoporous TiO_2 in conventional PSCs, despite the fact that the electron transfer between $MAPbI_3$ and TiO_2 was not improved and no attempt was made to select CNTs of any particular electronic type or chirality. This highlights that common arguments such as enhanced charge transport, are not always the largest contributing factor towards an improvement in device performance. The findings in this work provide new fundamental insights into the origin of the performance enhancements that can be achieved by the incorporation of carbon nanomaterials into the ETL of PSCs.

4. Experimental Section

Materials: All materials were purchased from Sigma, UK unless otherwise noted. Fluorine-doped tin oxide (FTO), TEC15 was purchased from Hartford Glass Co, USA. Transparent titania paste (18NR-T) and methyl ammonium iodide (CH_3NH_3I) were purchased from GreatCell Solar, Australia. Lead iodide (PbI_2) was purchased from Tokyo Chemical Industry, UK. Arc-discharge SWCNTs (P3-SWNT) were purchased from Carbon Solution Inc., USA. Poly[bis(4-phenyl)(2,4,6-trimethylphenyl)amine Poly(triarylamine) (PTAA) was purchased from Ossila, UK (batch M12, MW 27,381).

Preparation of TiO_2 -CNT composite solution: CNTs were initially prepared as a 1 vol% stock solution in Triton X-100. CNTs (10 mg) were dispersed in the prepared Triton X-100 solution (10 mL) using ultrasonication (bath) for 1 h. The concentration of the CNTs stock solution was

1 mg mL⁻¹. For the preparation of TiO₂-CNTs hybrid-based solutions, the desired concentration of 0.1 wt% of CNTs in the hybrid was obtained by adding an appropriate volume of the CNTs stock solution into 150 mg mL⁻¹ of transparent titania paste (18-NR-T) in ethanol. To ensure the concentration of TiO₂ particles remained equal for control and composite devices, the same volume of deionized water (as SWCNTs) was added to control samples.

Preparation of devices: FTO was first etched using 2M HCl and zinc followed by sequential cleaning in detergent, deionized water, acetone, ethanol, and isopropanol, and then finally treated with oxygen plasma for 10 min. A compact layer of TiO₂ (cp-TiO₂) was then deposited onto the FTO by spin coating a solution of 0.1M titanium diisopropoxide bis(acetylacetonate) (75 wt% in isopropanol), in 1-butanol at 3000 rpm for 20 s. After spin coating, the substrates were immediately heated at 150 °C for 2 min. This process was done in air and repeated twice to ensure a dense blocking layer was formed without pinholes. The cp-TiO₂ layer was then heated to 500 °C at a ramp rate of 50 °C min⁻¹ and left at 500 °C for 25 minutes. Transparent Titania Paste (18-NR-T) was diluted in ethanol at 150 mg mL⁻¹ and spin coated at 4000 rpm for 20 s on top of the cp-TiO₂ forming a mesoporous scaffold (mp-TiO₂). For films/devices containing the SWCNTs, 0.1 wt% of P3-SWCNTs was added to a 150 mg mL⁻¹ solution of 18-NR-T in ethanol. To ensure the same thickness of the mesoporous layer was maintained for both samples, the same volume of DI water was added to the control samples. The substrates were then heated to 500 °C at a ramp rate of 50 °C min⁻¹ and left at 500 °C for 25 min. Once the substrates had cooled, they were then doped with lithium by spin coating a 0.1M solution of bis(trifluoromethane)sulfonimide lithium salt (LiTFSI) in acetonitrile at 3000 rpm for 20 s and heated again to 500 °C following the same ramp rate and time as the mp-TiO₂. The substrates were then transferred to a nitrogen filled glovebox ready for perovskite deposition. The perovskite solution was prepared with slight modification to procedure previously reported in the literature by Ahn et al.^[63] Briefly, the CH₃NH₃I•PbI₂•DMSO adduct solution was

prepared by mixing 461 mg of PbI_2 and 159 mg of $\text{CH}_3\text{NH}_3\text{I}$ with 600 mg of DMF and 78 mg of DMSO. The solution was stirred in a nitrogen filled glovebox for 1 h at 65 °C and filtered before use. The filtered solution was spin coated on the previously prepared TiO_2 films at 5000 rpm for 30 s and after 7 s had elapsed, 0.5 mL of diethyl ether was slowly dripped onto the rotating substrate. The transparent $\text{CH}_3\text{NH}_3\text{I}\cdot\text{PbI}_2\cdot\text{DMSO}$ adduct film was heated to 65 °C for 2 min and 100 °C for 10 min to obtain a dense $\text{CH}_3\text{NH}_3\text{PbI}_3$ film. For the hole transport material (HTM), a 10 mg mL^{-1} solution of PTAA in toluene was prepared by stirring in a nitrogen filled glovebox for 1 h at 65 °C. The fully dissolved solution was then doped with additives of 7.5 μL bis(trifluoromethane)sulfonimide lithium salt (Li-TFSI)/acetonitrile (170 mg mL^{-1}) and 4 μL of 4-tert-butylpyridine (tBP). Finally, 80 nm of Au was thermally evaporated as a counter electrode. The thickness of the layers in the perovskite solar cell can be seen in Scheme 1 and are as follows: cp- TiO_2 (30 nm), mp- TiO_2 + perovskite (500 nm), PTAA (80 nm), and Au (80 nm). For the stability measurements, the devices were not encapsulated and measured under constant illumination (AM 1.5) under ambient conditions with humidity levers between 40-50%.

Film characterization: All samples were aged for 12 days in a nitrogen-filled glovebox in the dark at room temperature to avoid any surface reconstruction and ripening effects during the experiments.^[68,75] The steady-state photoluminescence and absorption spectra were obtained using a Horiba FL 1039 and Shimadzu UV-2600. The stability of samples was checked before and after TAS and TCSPC experiments by means of photoluminescence and absorbance spectroscopy. Time-correlated single photon counting (TCSPC) was carried out on a Horiba Delta Flex system. The excitation was 635 nm with a 200 ps pulse duration with a 1 MHz repetition rate. The PL transient signal was collected using a single-photon counting detectors (PPD-900, Horiba) with a 100 ns time window. Ultrafast transient absorption spectroscopy (fs-TAS) was recorded on a HELIOS transient absorption spectrometer (Ultrafast systems) with a

715 nm excitation source that was generated by an optical amplifier (TOPAS Prime, Spectra-Physics) and a frequency mixer (NirUVis, Light Conversion) and a probe pulse generated in a sapphire crystal. A Solstice Ti:Sapphire regenerative amplifier (Newport, Spectra-Physics) was used as a seeder with a system response time of 200 fs. The excitation density of the pump beam was modulated using a graded neutral density filter from 0.25 to 50 $\mu\text{J cm}^{-2}$ pulse energies at a repetition rate of 500 Hz, monitored with a VEGA energy meter (OPHIR Photonics). Scanning electron microscope (SEM) images were obtained using a LEO Gemini 1525 field emission gun scanning electron microscope with a fixed operating voltage of 5 kV. Raman scattering spectra and confocal Raman spectral images were taken using an alpha300R (WiTEC, Germany) microscope operating in Raman mode, equipped with a 532 nm laser ($E_{\text{laser}}=2.33$ eV) and a 40x objective (Numerical Aperture 0.6) with laser power levels kept constant during each experiment.

Photovoltaic measurements: J - V measurements were performed under one sun (AM 1.5G) illumination using a calibrated solar simulator with a Xenon lamp (LOT). Devices were connected to a Keithley 2400 source meter to measure the output. IPCE measurements were obtained with a halogen lamp chopped to a frequency of 188 Hz through a Newport monochromator and a 4-point probe in connection with a lock-in amplifier was used to collect data. The monochromatic beam was calibrated using a silicon photo-diode and the data was analyzed with Tracer 3.2 software (LOT) to produce the EQE spectra. Electrochemical impedance spectroscopy (EIS) measurements were performed on a Gamry electrochemical workstation (Gamry Interface 1000). The EIS measurements were performed at an applied bias of -0.700 V with a sinusoidal signal over a frequency range from 0.01 Hz to 100 kHz in the dark.

Other characterization: Ellipsometric measurements were performed using an SE-2000 spectroscopic ellipsometer (Semilabs, Hungary). Ellipsometric parameters were measured with illumination angles of 70° and 65° for both TiO₂-CNTs and TiO₂. Optical constants were derived for both materials by fitting the measured data from both angles of incidence simultaneously with a pair of Tauc-Lorentz oscillators. X-ray diffraction: X-Ray diffraction (XRD) patterns were recorded using a Bruker D8 Discover X-ray diffractometer using monochromatic Cu *K*_{α1} and Cu *K*_{α2} radiation of wavelengths 1.54056 and 1.54439 Å respectively.

Supporting Information

Acknowledgements

T.J.M would like to acknowledge the Ramsay Memorial Trust for their financial assistance.

T.J.M and I.P.P acknowledge the Engineering and Physical Sciences Research Council (EPSRC) for their financial support (EP/L015862/1). The authors would like to thank Dr. Piers

R F Barnes for the useful discussions.

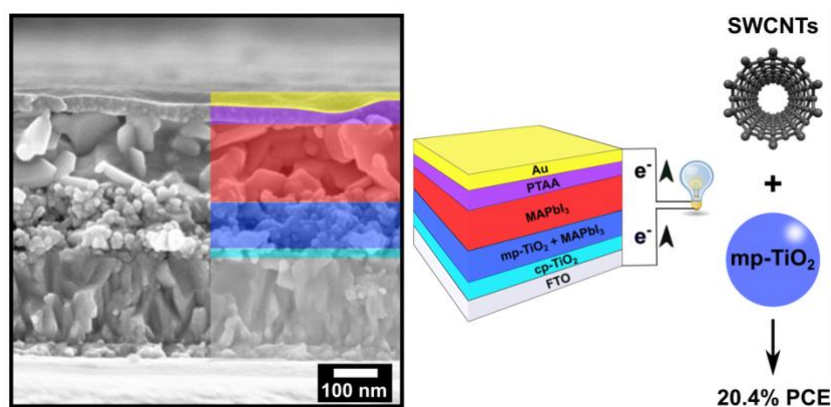
References

- [1] S. Khasminskaya, F. Pyatkov, K. Słowik, S. Ferrari, O. Kahl, V. Kovalyuk, P. Rath, A. Vetter, F. Hennrich, M. M. Kappes, G. Gol'tsman, A. Korneev, C. Rockstuhl, R. Krupke, W. H. P. Pernice, *Nature Photonics* **2016**, *10*, 727.
- [2] X. He, H. Htoon, S. K. Doorn, W. H. P. Pernice, F. Pyatkov, R. Krupke, A. Jeantet, Y. Chassagneux, C. Voisin, *Nature Materials* **2018**, *17*, 663.
- [3] M. S. Fuhrer, J. Nygård, L. Shih, M. Forero, Y.-G. Yoon, M. S. C. Mazzoni, H. J. Choi, J. Ihm, S. G. Louie, A. Zettl, P. L. McEuen, *Science* **2000**, *288*, 494–497.
- [4] D. Zhong, Z. Zhang, L. Ding, J. Han, M. Xiao, J. Si, L. Xu, C. Qiu, L.-M. Peng, *Nature Electronics* **2018**, *1*, 40–45.
- [5] J. Chen, M. A. Hamon, H. Hu, Y. Chen, A. M. Rao, P. C. Eklund, R. C. Haddon, *Science* **1998**, *282*, 95–98.

- [6] L.-M. Peng, Z. L. Zhang, Z. Q. Xue, Q. D. Wu, Z. N. Gu, D. G. Pettifor, *Phys. Rev. Lett.* **2000**, *85*, 3249–3252.
- [7] R. H. Baughman, A. A. Zakhidov, W. A. de Heer, *Science* **2002**, *297*, 787–792.
- [8] K. M. Liew, C. H. Wong, X. Q. He, M. J. Tan, *Phys. Rev. B* **2005**, *71*, 075424.
- [9] H. Ago, K. Petritsch, M. S. P. Shaffer, A. H. Windle, R. H. Friend, *Advanced Materials* **1999**, *11*, 1281–1285.
- [10] K. Jung, J. S. Hong, R. Vittal, K.-J. Kim, *Chem. Lett.* **2002**, *31*, 864–865.
- [11] K. Suzuki, M. Yamaguchi, M. Kumagai, S. Yanagida, *Chem. Lett.* **2002**, *32*, 28–29.
- [12] B. J. Landi, R. P. Raffaele, S. L. Castro, S. G. Bailey, *Progress in Photovoltaics: Research and Applications* **2005**, *13*, 165–172.
- [13] D. D. Tune, F. Henrich, S. Dehm, M. F. G. Klein, K. Glaser, A. Colsmann, J. G. Shapter, U. Lemmer, M. M. Kappes, R. Krupke, B. S. Flavel, *Advanced Energy Materials* **2013**, *3*, 1091–1097.
- [14] M. Gong, T. A. Shastry, Y. Xie, M. Bernardi, D. Jasion, K. A. Luck, T. J. Marks, J. C. Grossman, S. Ren, M. C. Hersam, *Nano Lett.* **2014**, *14*, 5308–5314.
- [15] M. Pfohl, K. Glaser, A. Graf, A. Mertens, D. D. Tune, T. Puerckhauer, A. Alam, L. Wei, Y. Chen, J. Zaumseil, A. Colsmann, R. Krupke, B. S. Flavel, *Advanced Energy Materials* **2016**, *6*, 1600890.
- [16] F. D'Souza, O. Ito, *Chem. Soc. Rev.* **2011**, *41*, 86–96.
- [17] D. D. Tune, J. G. Shapter, *Energy Environ. Sci.* **2013**, *6*, 2572–2577.
- [18] M. Batmunkh, M. J. Biggs, J. G. Shapter, *Small* **2015**, *11*, 2963–2989.
- [19] S. N. Habisreutinger, B. Wenger, H. J. Snaith, R. J. Nicholas, *ACS Energy Letters* **2017**, *2*, 622–628.
- [20] M. Batmunkh, T. J. Macdonald, C. J. Shearer, M. Bat-Erdene, Y. Wang, M. J. Biggs, I. P. Parkin, T. Nann, J. G. Shapter, *Advanced Science* **2017**, *4*, DOI 10.1002/advs.201600504.
- [21] M. Batmunkh, C. J. Shearer, M. Bat-Erdene, M. J. Biggs, J. G. Shapter, *ACS Applied Materials & Interfaces* **2017**, *9*, 19945–19954.
- [22] M. Batmunkh, C. J. Shearer, M. J. Biggs, J. G. Shapter, *J. Mater. Chem. A* **2015**, *3*, 9020–9031.
- [23] S. N. Habisreutinger, R. J. Nicholas, H. J. Snaith, *Advanced Energy Materials* **2017**, *7*, DOI 10.1002/aenm.201601839.
- [24] Z. Wei, H. Chen, K. Yan, X. Zheng, S. Yang, *J. Mater. Chem. A* **2015**, *3*, 24226–24231.
- [25] I. Jeon, S. Seo, Y. Sato, C. Delacou, A. Anisimov, K. Suenaga, E. I. Kauppinen, S. Maruyama, Y. Matsuo, *J. Phys. Chem. C* **2017**, *121*, 25743–25749.
- [26] D. P. McMeekin, G. Sadoughi, W. Rehman, G. E. Eperon, M. Saliba, M. T. Hörlantner, A. Haghighirad, N. Sakai, L. Korte, B. Rech, M. B. Johnston, L. M. Herz, H. J. Snaith, *Science* **2016**, *351*, 151–155.
- [27] T. J. Macdonald, D. D. Tune, M. R. Dewi, C. T. Gibson, J. G. Shapter, T. Nann, *ChemSusChem* **2015**, *8*, 3396–3400.
- [28] M. Batmunkh, T. J. Macdonald, C. J. Shearer, M. Bat-Erdene, Y. Wang, M. J. Biggs, I. P. Parkin, T. Nann, J. G. Shapter, *Advanced Science* **2017**, *4*, 1600504.
- [29] L. Yang, W. W.-F. Leung, *Advanced Materials* **2013**, *25*, 1792–1795.
- [30] K. Woan, G. Pyrgiotakis, W. Sigmund, *Advanced Materials* **2009**, *21*, 2233–2239.
- [31] G. K. Mor, K. Shankar, M. Paulose, O. K. Varghese, C. A. Grimes, *Nano Lett.* **2006**, *6*, 215–218.
- [32] P. Schulz, A.-M. Dowgiallo, M. Yang, K. Zhu, J. L. Blackburn, J. J. Berry, *J. Phys. Chem. Lett.* **2016**, *7*, 418–425.
- [33] W. S. Yang, B.-W. Park, E. H. Jung, N. J. Jeon, Y. C. Kim, D. U. Lee, S. S. Shin, J. Seo, E. K. Kim, J. H. Noh, S. I. Seok, *Science* **2017**, *356*, 1376–1379.

- [34] J. A. Christians, P. Schulz, J. S. Tinkham, T. H. Schloemer, S. P. Harvey, B. J. T. de Villers, A. Sellinger, J. J. Berry, J. M. Luther, *Nature Energy* **2018**, *3*, 68–74.
- [35] P. Holzhey, P. Yadav, S.-H. Turren-Cruz, M. Grätzel, A. Hagfeldt, M. Saliba, *Materials Today* **2018**, DOI 10.1016/j.mattod.2018.10.017.
- [36] S. N. Habisreutinger, N. K. Noel, H. J. Snaith, *ACS Energy Lett.* **2018**, *3*, 2472–2476.
- [37] K.-H. Jung, J.-Y. Seo, S. Lee, H. Shin, N.-G. Park, *J. Mater. Chem. A* **2017**, *5*, 24790–24803.
- [38] J.-W. Lee, S.-G. Kim, S.-H. Bae, D.-K. Lee, O. Lin, Y. Yang, N.-G. Park, *Nano Lett.* **2017**, *17*, 4270–4276.
- [39] P. P. Boix, K. Nonomura, N. Mathews, S. G. Mhaisalkar, *Materials Today* **2014**, *17*, 16–23.
- [40] F. Giordano, A. Abate, J. P. C. Baena, M. Saliba, T. Matsui, S. H. Im, S. M. Zakeeruddin, M. K. Nazeeruddin, A. Hagfeldt, M. Graetzel, *Nature Communications* **2016**, *7*, ncomms10379.
- [41] A. J. Huckaba, S. Gharibzadeh, M. Ralaiarisoa, C. Roldán-Carmona, N. Mohammadian, G. Grancini, Y. Lee, P. Amsalem, E. J. Plichta, N. Koch, A. Moshaii, M. K. Nazeeruddin, *Small Methods* **2017**, *1*, 1700250.
- [42] M. N. F. Hoque, N. Islam, Z. Li, G. Ren, K. Zhu, Z. Fan, *ChemSusChem* **2016**, *9*, 2692–2698.
- [43] Y. Shao, Z. Xiao, C. Bi, Y. Yuan, J. Huang, *Nature Communications* **2014**, *5*, 5784.
- [44] T.-Y. Yang, G. Gregori, N. Pellet, M. Grätzel, J. Maier, *Angewandte Chemie* **2015**, *127*, 8016–8021.
- [45] M. Bag, L. A. Renna, R. Y. Adhikari, S. Karak, F. Liu, P. M. Lahti, T. P. Russell, M. T. Tuominen, D. Venkataraman, *J. Am. Chem. Soc.* **2015**, *137*, 13130–13137.
- [46] A. Dualeh, T. Moehl, M. K. Nazeeruddin, M. Grätzel, *ACS Nano* **2013**, *7*, 2292–2301.
- [47] A. K. Chandiran, A. Yella, M. T. Mayer, P. Gao, M. K. Nazeeruddin, M. Grätzel, *Advanced Materials* **2014**, *26*, 4309–4312.
- [48] M. M. Lee, J. Teuscher, T. Miyasaka, T. N. Murakami, H. J. Snaith, *Science* **2012**, *338*, 643.
- [49] J. Yin, J. Cao, X. He, S. Yuan, S. Sun, J. Li, N. Zheng, L. Lin, *J. Mater. Chem. A* **2015**, *3*, 16860–16866.
- [50] Y. Du, H. Cai, Y. Wu, Z. Xing, Z. Li, J. Xu, L. Huang, J. Ni, J. Li, J. Zhang, *Phys. Chem. Chem. Phys.* **2017**, *19*, 13679–13686.
- [51] Y.-C. Ho, M. N. F. Hoque, E. Stoneham, J. Warzywoda, T. Dallas, Z. Fan, *J. Phys. Chem. C* **2017**, *121*, 23939–23946.
- [52] T. J. Macdonald, F. Ambroz, M. Batmunkh, Y. Li, D. Kim, C. Contini, R. Poduval, H. Liu, J. G. Shapter, I. Papakonstantinou, I. P. Parkin, *Materials Today Energy* **2018**, *9*, 254–263.
- [53] E. Mosconi, J. M. Azpiroz, F. De Angelis, *Chem. Mater.* **2015**, *27*, 4885–4892.
- [54] Q. Guo, F. Yuan, B. Zhang, S. Zhou, J. Zhang, Y. Bai, L. Fan, T. Hayat, A. Alsaedi, Z. Tan, *Nanoscale* **2018**, *11*, 115–124.
- [55] P. G. Collins, K. Bradley, M. Ishigami, A. Zettl, *Science* **2000**, *287*, 1801–1804.
- [56] K. Wojciechowski, T. Leijtens, S. Siprova, C. Schlueter, M. T. Hörantner, J. T.-W. Wang, C.-Z. Li, A. K.-Y. Jen, T.-L. Lee, H. J. Snaith, *J. Phys. Chem. Lett.* **2015**, *6*, 2399–2405.
- [57] A. Sadollahkhani, P. Liu, V. Leandri, M. Safdari, W. Zhang, J. M. Gardner, *ChemPhysChem* **2017**, *18*, 3047–3055.
- [58] A. S. R. Bati, L. Yu, S. A. Tawfik, M. J. S. Spencer, P. E. Shaw, M. Batmunkh, J. G. Shapter, *iScience* **2019**, *14*, 100–112.
- [59] B. Kilic, S. Turkdogan, A. Astam, O. C. Ozer, M. Asgin, H. Cebeci, D. Urk, S. P. Mucur, *Scientific Reports* **2016**, *6*, 27052.

- [60] C. Dette, M. A. Pérez-Osorio, C. S. Kley, P. Punke, C. E. Patrick, P. Jacobson, F. Giustino, S. J. Jung, K. Kern, *Nano Lett.* **2014**, *14*, 6533–6538.
- [61] Y. Bai, Q. Dong, Y. Shao, Y. Deng, Q. Wang, L. Shen, D. Wang, W. Wei, J. Huang, *Nature Communications* **2016**, *7*, 12806.
- [62] Y.-J. Shi, R.-J. Zhang, H. Zheng, D.-H. Li, W. Wei, X. Chen, Y. Sun, Y.-F. Wei, H.-L. Lu, N. Dai, L.-Y. Chen, *Nanoscale Research Letters* **2017**, *12*, 243.
- [63] N. Ahn, D.-Y. Son, I.-H. Jang, S. M. Kang, M. Choi, N.-G. Park, *Journal of the American Chemical Society* **2015**, *137*, 8696–8699.
- [64] Y. Yamada, T. Yamada, L. Q. Phuong, N. Maruyama, H. Nishimura, A. Wakamiya, Y. Murata, Y. Kanemitsu, *Journal of the American Chemical Society* **2015**, *137*, 10456–10459.
- [65] J. Kim, R. Godin, S. D. Dimitrov, T. Du, D. Bryant, M. A. McLachlan, J. R. Durrant, *Advanced Energy Materials* **2018**, 1802474.
- [66] J.-W. Lee, H.-S. Kim, N.-G. Park, *Acc. Chem. Res.* **2016**, *49*, 311–319.
- [67] D. Shi, V. Adinolfi, R. Comin, M. Yuan, E. Alarousu, A. Buin, Y. Chen, S. Hoogland, A. Rothenberger, K. Katsiev, Y. Losovyj, X. Zhang, P. A. Dowben, O. F. Mohammed, E. H. Sargent, O. M. Bakr, *Science* **2015**, *347*, 519–522.
- [68] Y. Yamada, T. Yamada, A. Shimazaki, A. Wakamiya, Y. Kanemitsu, *J. Phys. Chem. Lett.* **2016**, *7*, 1972–1977.
- [69] A. R. Pascoe, M. Yang, N. Kopidakis, K. Zhu, M. O. Reese, G. Rumbles, M. Fekete, N. W. Duffy, Y.-B. Cheng, *Nano Energy* **2016**, *22*, 439–452.
- [70] A. K. Rumaiz, J. C. Woicik, E. Cockayne, H. Y. Lin, G. H. Jaffari, S. I. Shah, *Appl. Phys. Lett.* **2009**, *95*, 262111.
- [71] A. Kuznetsova, I. Popova, Yates John T., M. J. Bronikowski, C. B. Huffman, J. Liu, R. E. Smalley, H. H. Hwu, J. G. Chen, *J. Am. Chem. Soc.* **2001**, *123*, 10699–10704.
- [72] S. Ayissi, P. A. Charpentier, K. Palotás, N. Farhangi, F. Schwarz, W. A. Hofer, *J. Phys. Chem. C* **2015**, *119*, 15085–15093.
- [73] T. Du, C. H. Burgess, J. Kim, J. Zhang, J. R. Durrant, M. A. McLachlan, *Sustainable Energy Fuels* **2017**, *1*, 119–126.



Scheme 1. Scross-section SEM of a conventional device architecture containing CNTs.

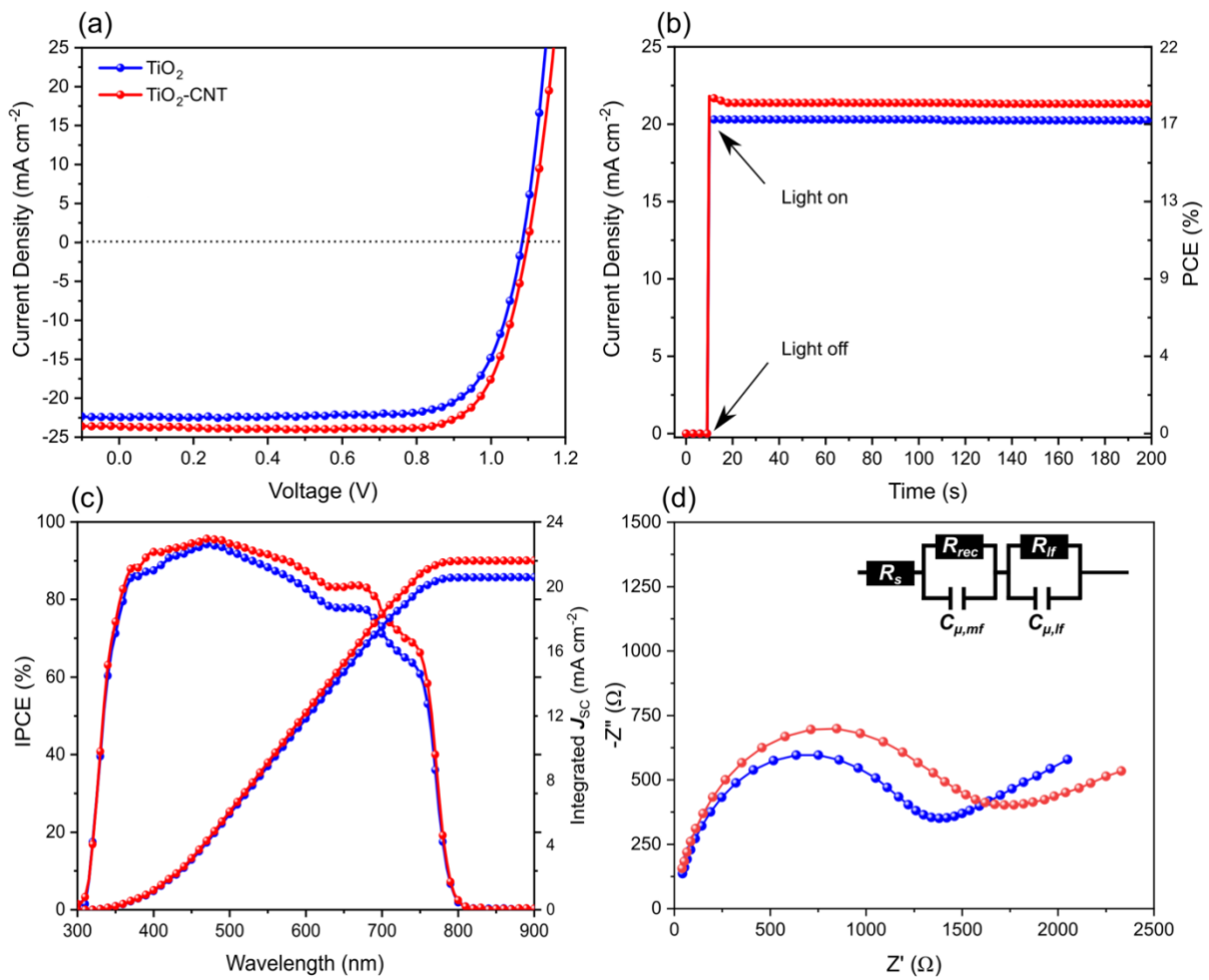


Figure 1. (a) JV curves, (b) PSCs held at near MPP to measure their steady-state PCE (c) IPCE and integrated current density, (d) Nyquist plot of the electrochemical impedance of TiO₂-CNT and TiO₂ PSCs

Table 1. Photovoltaic parameters extracted from the J-V curves for TiO₂-CNT and TiO₂ PSCs.

Photoelectrode	J_{SC} (mA cm ⁻²)	V_{OC} (V)	FF	PCE (%)
TiO ₂	22.4 21.4 (+/- 0.16)	1.08 1.05 (+/- 0.003)	0.76 0.71 (+/- 0.04)	18.4 16.0 (+/- 0.15)
TiO ₂ -CNT	23.6 22.9 (+/- 0.11)	1.10 1.07 (+/- 0.003)	0.79 0.73 (+/- 0.05)	20.4 18.0 (+/- 0.15)

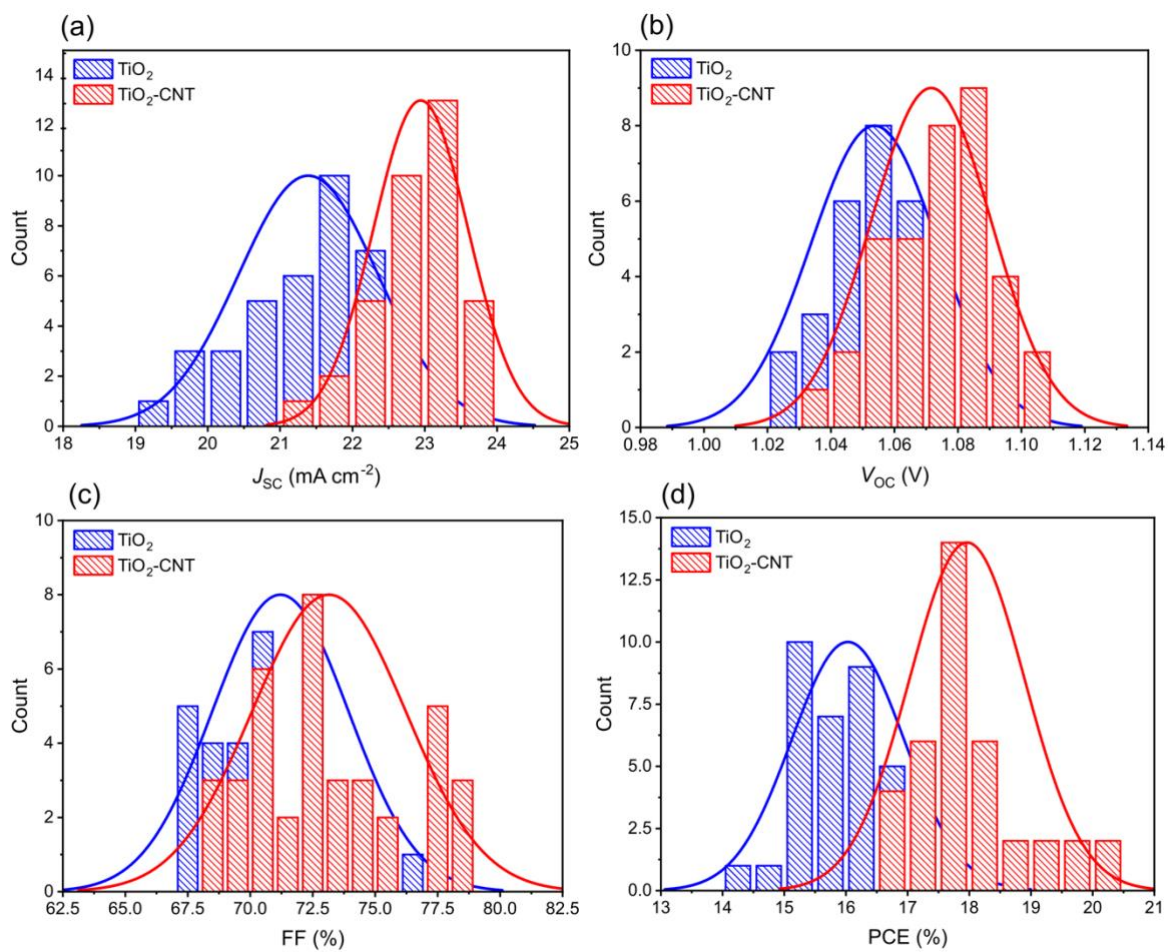


Figure 2. Histograms of photovoltaic parameters J_{sc} (a), V_{oc} (b), FF (c), and PCE (d) for TiO_2 and $\text{TiO}_2\text{-CNT}$ PSCs. The histograms shown are the average parameters for 76 devices made over the course of 6 months.

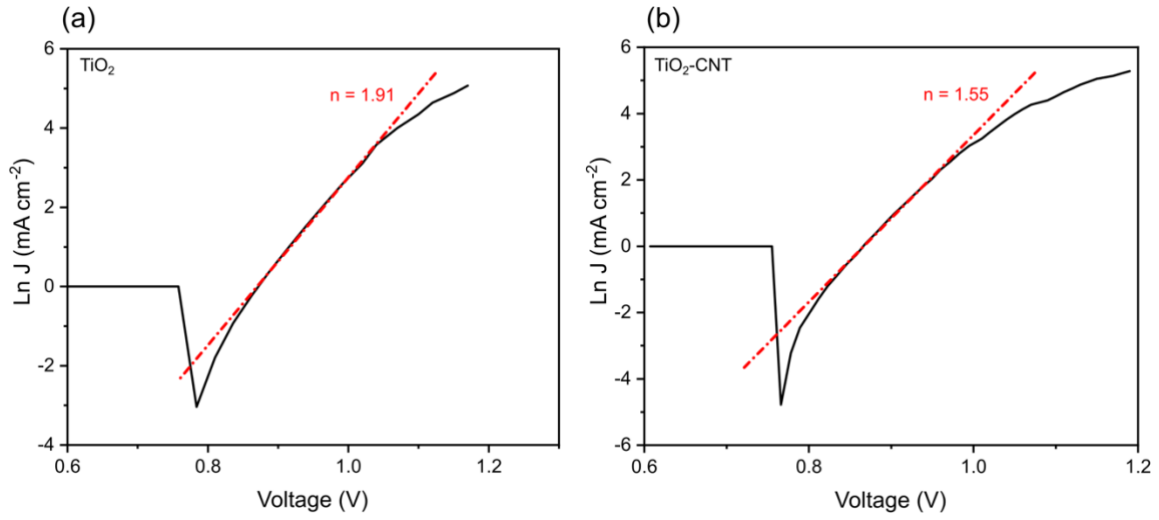


Figure 3. Semi-log plots of dark J - V measurements for (a) TiO_2 and (b) TiO_2 -CNT PSCs.

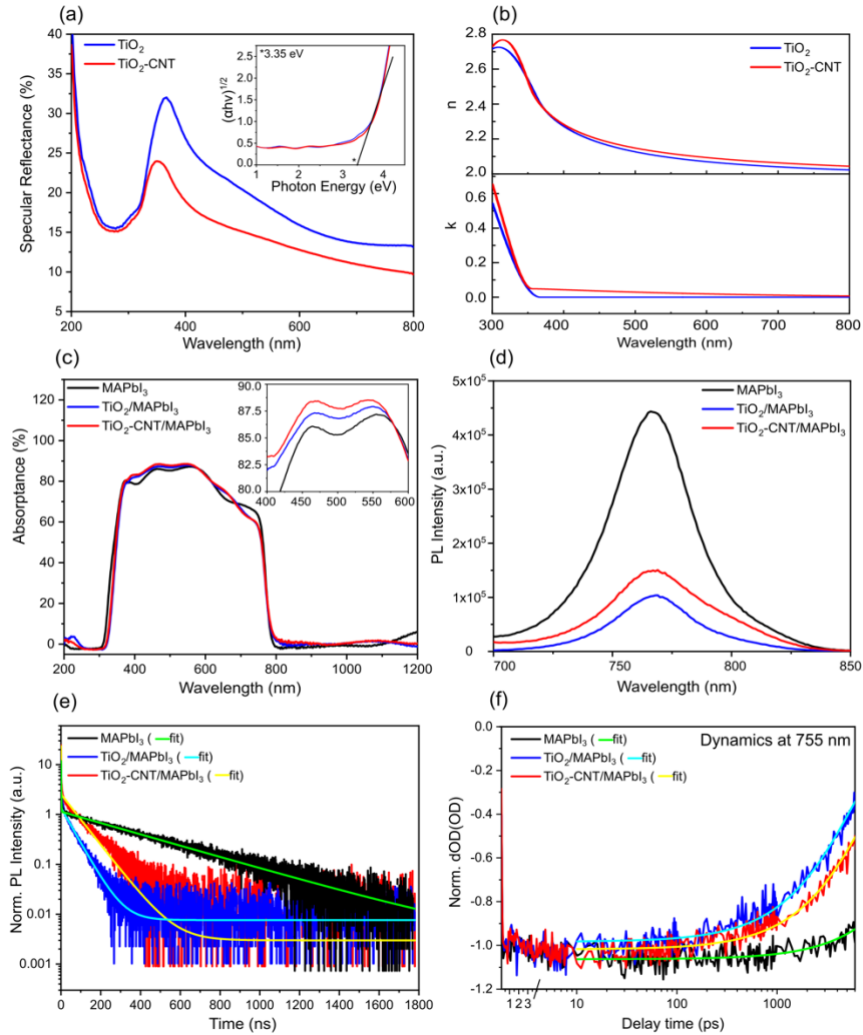


Figure 4. (a) Specular reflectance of TiO_2 and TiO_2 -CNT films, inset shows the Tauc plots of the data used to extract the bandgap, (b) complex refractive index of TiO_2 and TiO_2 -CNT films, extracted from the ellipsometry measurements, (c), (d), (e) and (f) show absorbance, PL, TCSPC, and fs-TAS, respectively, of MAPbI_3 (black), TiO_2 / MAPbI_3 (blue), and TiO_2 -CNT/ MAPbI_3 (red).

Table 2. Parameters for the biexponential fitting of the TCSPC data for MAPbI₃, TiO₂/MAPbI₃, and TiO₂-CNT/MAPbI₃ photoelectrodes. The percentage contribution factors for τ_1 and τ_2 from integrating under the traces are also quoted.

Photoelectrode	A ₁	τ_1 (ns)	A ₂	τ_2 (ns)	τ_1 (%)	τ_2 (%)
MAPbI ₃	10.7 (+/- 0.04)	0.85 (+/- 0.01)	1.14 (+/- 0.01)	380 (+/- 2.39)	8.4	91.6
TiO ₂ /MAPbI ₃	9.97 (+/- 0.07)	0.58 (+/- 0.01)	1.37 (+/- 0.01)	60.5 (+/- 0.83)	15.4	84.6
TiO ₂ - CNT/MAPbI ₃	21.1 (+/- 0.10)	0.73 (+/- 0.01)	2.15 (+/- 0.01)	97.4 (+/- 0.95)	17.6	82.4

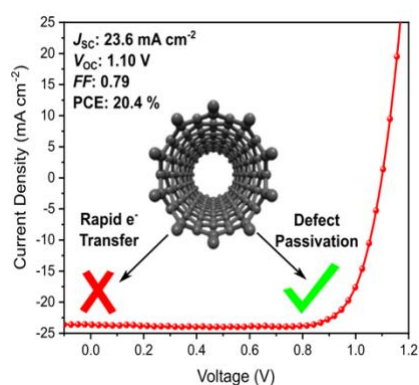
Device performance parameters of titanium dioxide/carbon nanotube composite perovskite solar cells are correlated with the spectroscopic signatures of the materials to determine the origin of performance enhancement. This study discusses new fundamental understandings for the role of carbon nanomaterials in perovskite solar cells and presents a significant step forward in advancing the field of high-performance photovoltaics.

Keyword: carbon nanotubes, perovskite solar cells, device performance, titanium dioxide, cnts

Thomas J. Macdonald, Munkhbayar Batmunkh, Chieh-Ting Lin, Jinhyun Kim, Daniel D. Tune, Filip Amboz, Xiaoe Li, Shengda Xu, Christian Sol, Ioannis Papakonstantinou, Martyn A. McLachlan, Ivan P. Parkin, Joseph G. Shapter, James R. Durrant*

Origin of Performance Enhancement in TiO₂-Carbon Nanotube Composite Perovskite Solar Cells

ToC figure ((Please choose one size: 55 mm broad × 50 mm high **or** 110 mm broad × 20 mm high. Please do not use any other dimensions))



Supporting Information

Origin of Performance Enhancement in TiO₂-Carbon Nanotube Composite Perovskite Solar Cells

*Thomas J. Macdonald**, Munkhbayar Batmunkh, Chieh-Ting Lin, Jinhyun Kim, Daniel D. Tune, Filip Amboz, Xiaoe Li, Shengda Xu, Christian Sol, Ioannis Papakonstantinou, Martyn A. McLachlan, Ivan P. Parkin, Joseph G. Shapter, James R. Durrant

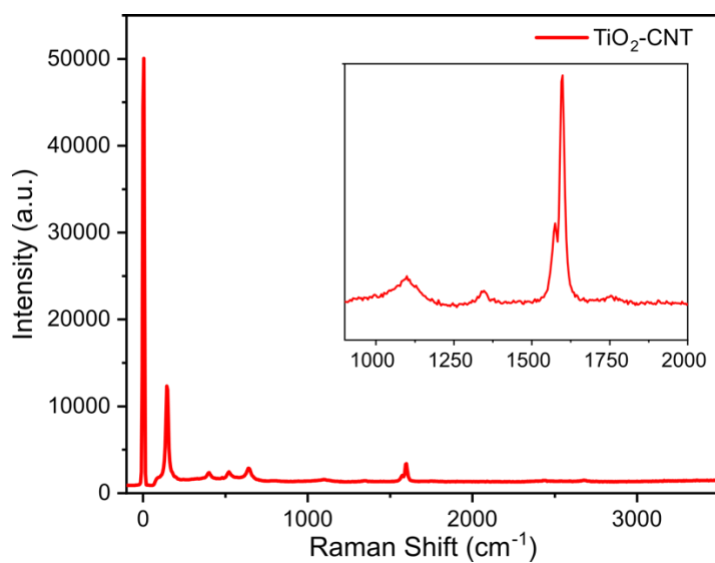


Figure S1. Raman spectroscopy verifying the presence of CNTs in the TiO₂ thin films.

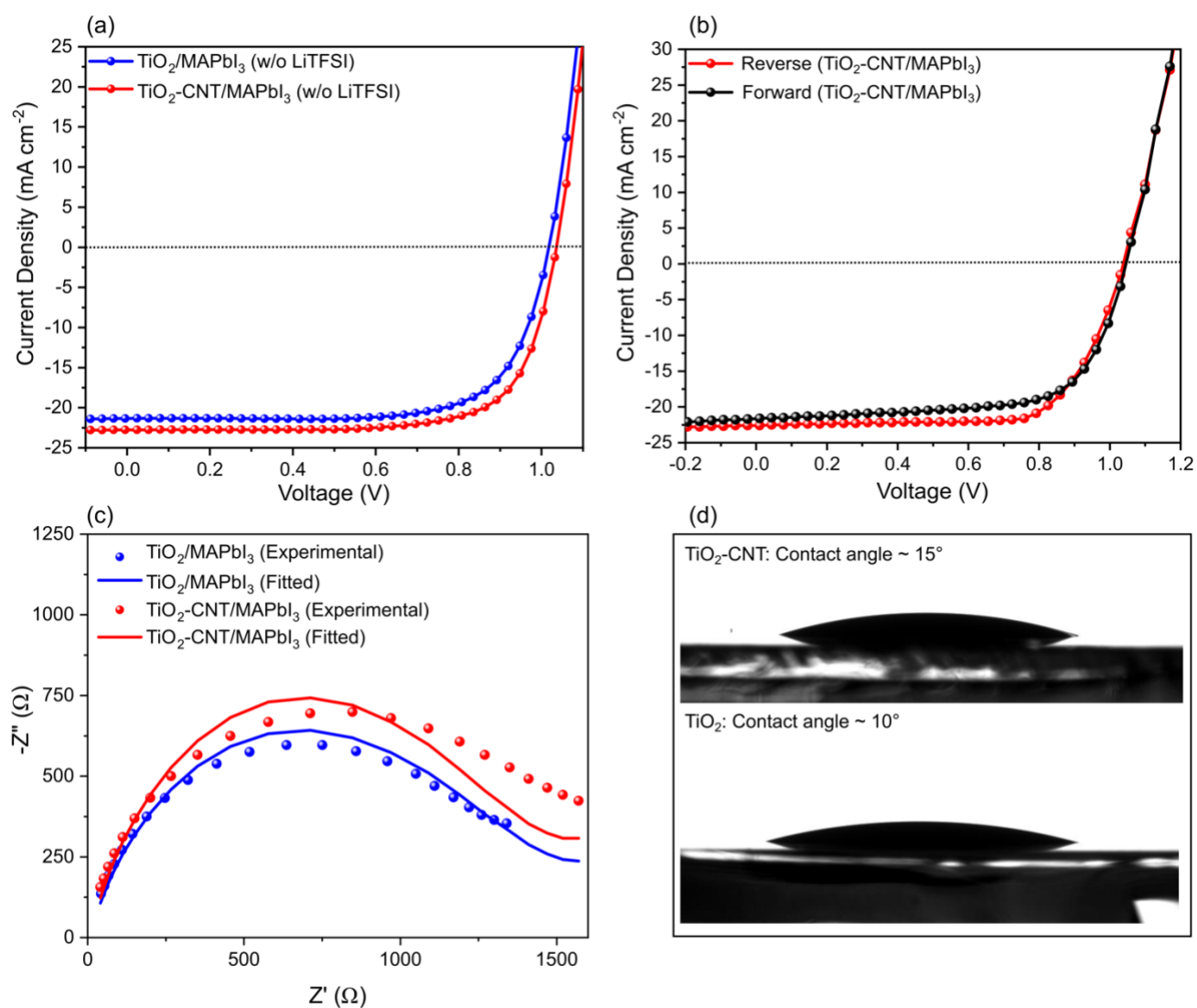


Figure S2. *J-V* curves for TiO₂-CNT and TiO₂ PSCs without LiTFSI treatment

Table S1. *J-V* parameters for TiO₂ and TiO₂-CNT PSCs without LiTFSI treatment

Photoelectrode	J_{SC} (mA cm ⁻²)	V_{oc} (V)	FF	PCE (%)
TiO ₂ (w/o LiTFSI)	21.3 (+/- 0.1)	1.02 (+/- 0.003)	0.72 (+/- 0.04)	15.6 (+/- 0.1)
TiO ₂ -CNT (w/o LiTFSI)	22.7 (+/- 0.1)	1.04 (+/- 0.003)	0.73 (+/- 0.04)	17.2 (+/- 0.1)

Table S2. EIS parameters for TiO₂ and TiO₂-CNT PSCs measured under illumination at open circuit conditions

Photoelectrode	R_s (Ω)	R_{rec} (Ω)	C_{mf} (μF)	τ (μs)
TiO ₂	45.2 (+/- 2.5)	1389 (+/- 9.4)	1.5×10^{-2} (+/- 1.5×10^{-4})	21.2 (+/- 0.2)
TiO ₂ -CNT	40.4 (+/- 2.8)	1596 (+/- 11.2)	1.3×10^{-2} (+/- 1.3×10^{-4})	21.3 (+/- 1.6)

Table S3. Series and shunt resistance extracted from the light jv curves and parameters from the dark curves. Note that a small imperfection in the dark enclosure allowed the equivalent of 0.1-0.2 % of the AM1.5G intensity into the enclosure, but that this does not qualitatively alter the significant differences between the two types of device.

Photoelectrode	R_s (Ω cm²)	R_{SH} (Ω cm²)	J_{sat} (mA cm⁻²)	Ideality factor	Schottky barrier height (Φ_{BE})
TiO ₂	1.9 5.2 (+/- 0.3)	2.2×10^4 3.0×10^3 (+/- 6.7×10^2)	1.02×10^{-7} (+/- 9.9×10^{-8})	1.91 (+/- 0.18)	1.05 (+/- 0.05)
TiO ₂ -CNT	2.1 4.8 (+/- 0.2)	5.6×10^4 9.9×10^3 (+/- 2.4×10^3)	5.8×10^{-10} (+/- 3.6×10^{-10})	1.55 (+/- 0.03)	1.15 (+/- 0.05)

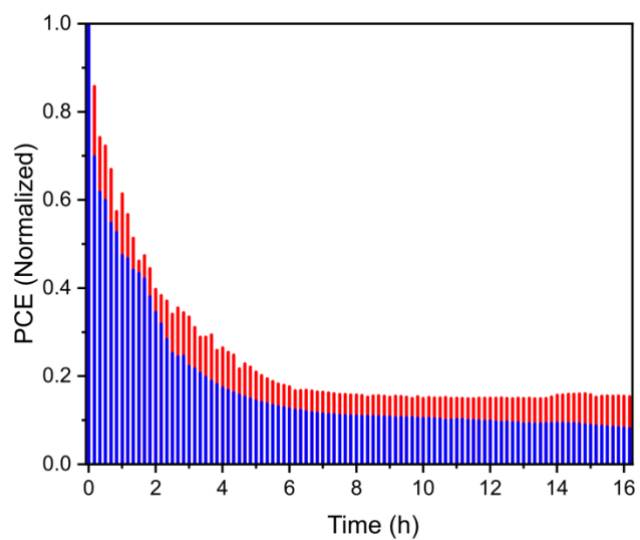


Figure S3. Stability measurements of PSCs held under constant 1-sun illumination for 16 h. J-V curves were measured periodically over a 16 h period.



Figure S4. TiO_2 and TiO_2 -CNT sol gel solutions used for the mp- TiO_2 layer in PSCs

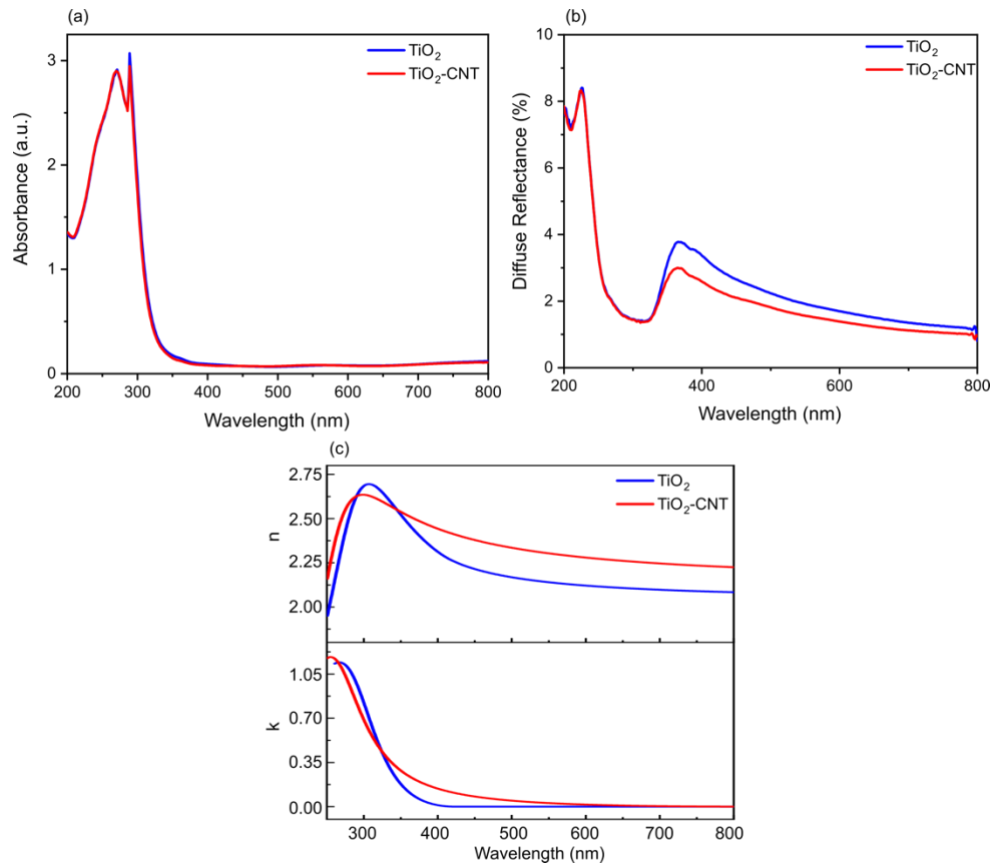


Figure S5. (a) Absorbance, (b) diffuse reflectance, (c) refractive index of TiO₂ and TiO₂-CNT photoelectrodes

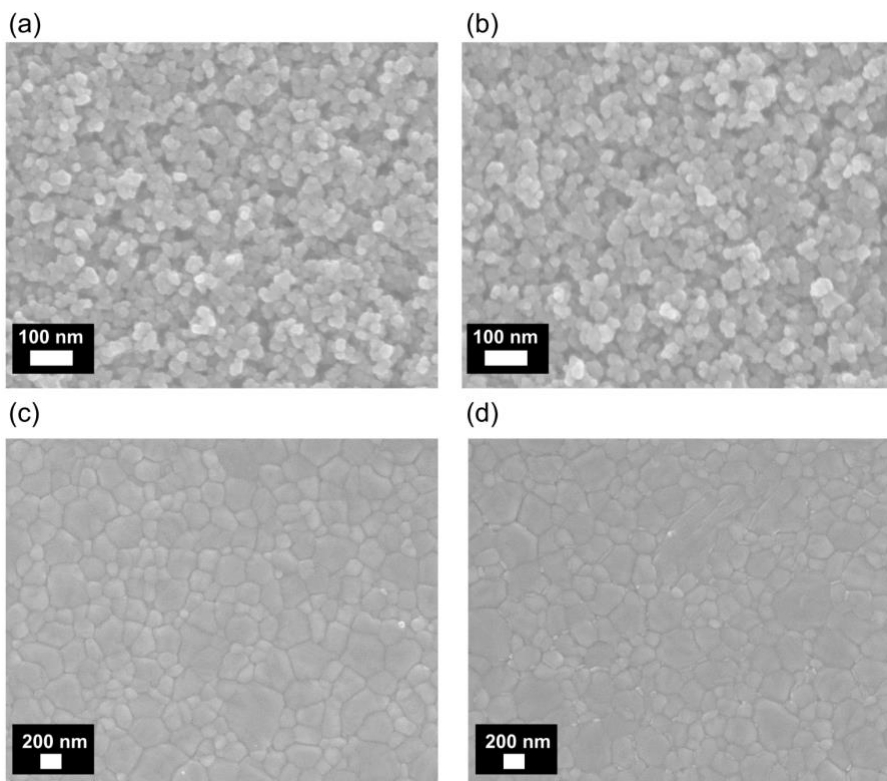


Figure S6. Topography SEM images. (a) TiO₂, (b) TiO₂-CNT, (c) TiO₂/MAPbI₃ and (d) TiO₂-CNT/MAPbI₃

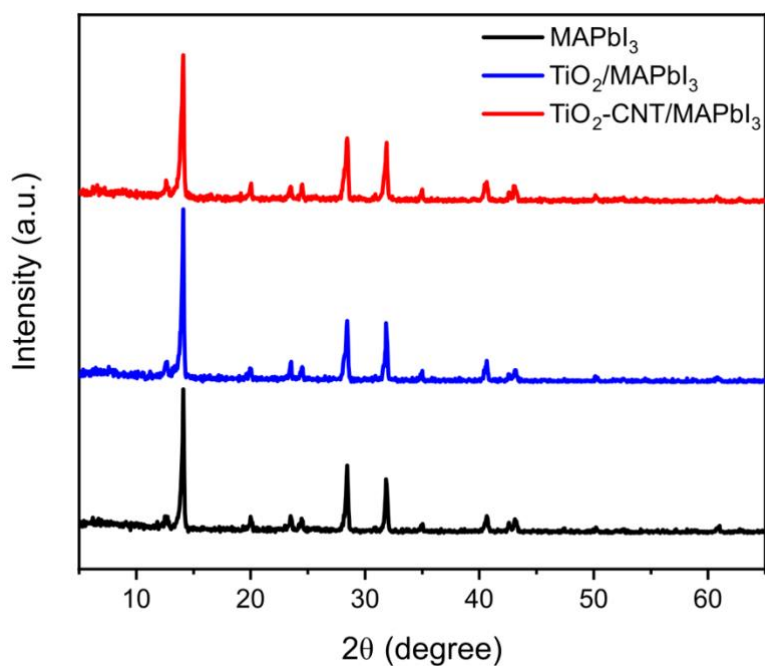


Figure S7. XRD of neat MAPbI₃, TiO₂/MAPbI₃, and TiO₂-CNT/MAPbI₃

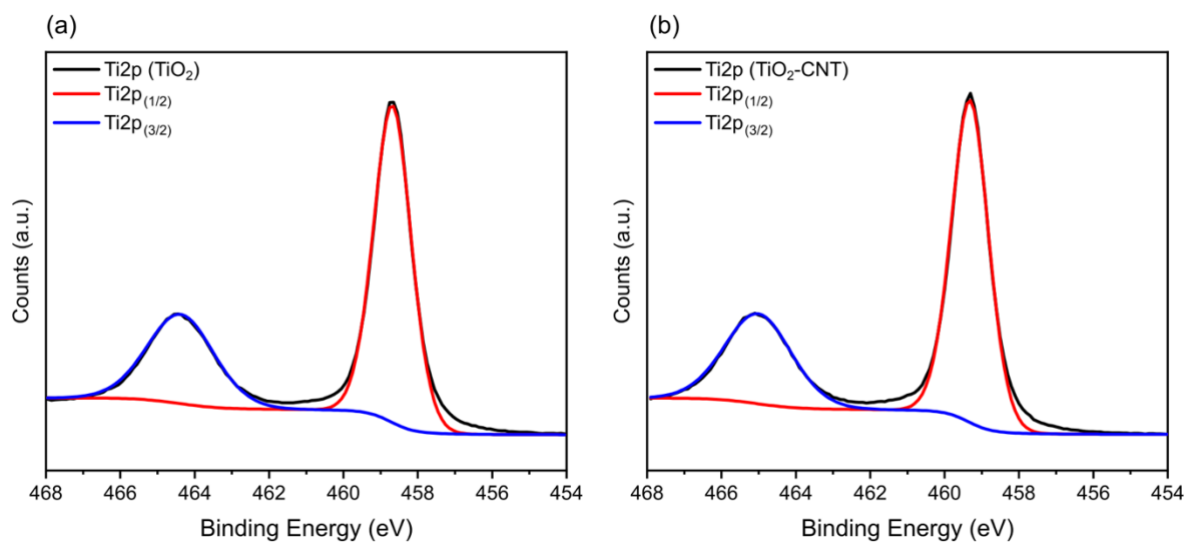


Figure S8. XPS of TiO₂ and TiO₂-CNT photoelectrodes